 doi:10.20944/preprints202209.0447.v1

Seismic signatures and site characterization of an intermittent stream in dry and flood conditions: an implication for soil losses and landslide triggering

Yawar Hussain[1*], Helena Seivane[2], Gao Qiangshan[3], Susanne Maciel[4], Omar Hamza[5], Rogério Uagoda[6] and Welitom Borges[7]

[1]Georisk & Environment, Department of Geology, University of Liege, Liege, 4000, Belgium
[2]Andalusian Institute of Geophysics and Earthquake Disaster Prevention, University of Granada, Granada, Spain
[3]State Key Laboratory of Space Weather, National Space Science Center, Chinese Academy of Sciences, Beijing, China
[4] Planaltina Campus, University of Brasília, Brasília, Brazil
[5]School of Built and Natural Environment, University of Derby, Derby, UK
[6]Department of Geography, University of Brasilia, Brasilia, Brazil
[7]Institute of Geosciences, University of Brasilia, Brasilia, Brazil
* Correspondence: author's email: yhussain@uliege.be

Abstract: The seasonal soil losses and frequent shallow landslides in the Cerrado region of Brazil have high destructive potential with social, economic, and climatic implications. As fluvial systems substantially drive such environmental threats; therefore, it is essential to conduct geological site characterization and continuously monitor the rivers' and streams' seasonal erosive potentials. However, in such unstable and sensitive conditions, traditional intrusive investigation approaches may not be safe, the geophysical investigation might offer a good alternative. For the present study, a geophysical approach (particularly the seismic method) was adopted to examine the seismic footprints and GPR site characterization of a seasonal stream in the Rua do Matto, Brasilia, Brazil. The monitoring was conducted (at a safe distance) on the intermittent stream over several durations of dry (no rain) and rainy (flood) conditions. After pre-processing the raw data, the power spectral density (PSDs) was computed as a function of several variables (wind speed), time-frequency spectrograms, ambient noise displacement root mean square (RMS), the single station horizontal-to-vertical spectral ratio (HVSR) curves. In addition, change-point analysis was used for comparing the ambient noise with wind speed (both were well correlated). The GPR amplitude and waveform variation features were attributed to the subsurface material and the presence of boulders in the floodplain and regions (low coherence value) susceptible to erosion (weak spots). The river flows were evident in the spectrograms, HVSR curves and different patterns of RMS displacements (at selective frequency ranges). The multi-peaks that emerged on the HVSR curve are further analyzed for changes in amplitude, width and troughs possibly related to river activities and soil moisture due to rain. The approach provides the basis for non-destructive monitoring tools enabling the detection of 'seismic signatures' and weak spots of the fluvial channels for improving environmental management.

Keywords: change-point analysis; weak spots; spectral analysis; ambient noise RMS; georadar attribute

1. Introduction

Due to climate change, floods and debris flow worldwide have increased riverbank erosion and landslides, impacting the downstream communities and causing severe losses in lives, properties, and land functionality [1,2]. Usually,

 doi:10.20944/preprints202209.0447.v1

local and small-scale erosions might not seem like serious instability problems. Still, in the long-term and extreme flood events, this situation often develops into landslides on riverbanks. It may also induce several issues, such as river blockage, a shift of river channel position, or flooding from rising riverbeds [3]. Consequently, it may lead to the collapse of roads and bridges built along the river network [4]. Therefore, monitoring riverbanks and erosive potential (EP) at an early stage is essential to inform the hazard evaluation and improve the risk management of erosion and landslide in such regions.

EP is adopted as an indicator of riverbank erosion and related hazards to aid the evaluation of the riverbanks' behavior. Fundamentally, EP is a function of various influencing factors, such as the rainfall intensity in the catchment area and the nature of sediment transport and incision [5]. EP is also affected by local site conditions that may include the degree of soil compaction (density), soil thickness, the topography of bedrock, and the presence of rock fragments. Therefore, EP assessment has a wide range of applications in landscape evolution, soil erosion, landslide, ecology, water quality, land use management, and civil and river engineering like dams and recreational reservoir silting [6–14]. These numerous geomorphological processes work at the background of the landscape evolution through undercutting and destabilization of the riverbanks. These are also coupled with geophysical processes, including the ambient noise wavefield, which can be a valuable source for monitoring. On the other hand, erosion and landslides are also highly influenced by the types and properties of soil, including density, porosity, and permeability, and any variation in these properties that represent potential shear plans [15]. Therefore, detecting such variations (weak spots) can be included within the scope of the monitoring work.

In the case of the Cerrado region of Brazil, erosion by water is a crucial soil threat [16–18]. The environmental dynamics in hydrographic basins, such as intensified erosion processes, siltation and decreased oxygen available in rivers and lakes, among other factors, may be inferred from the eroded sediments loads related to surface runoff and water infiltration into the soil [19]. The accurate monitoring and prediction of these sediment transportation as the EP of the river are challenging tasks with the currently adopted techniques such as (i) the stream hydrophones or geophones [20], (ii) identification of particles with a tracer or radiofrequency [21], and (iii) calculation via empirical relationships calibrated in the laboratory [22]. However, these techniques can be logistically challenging, particularly in significant flooding events, and so their application becomes cost-prohibitive [23]. With the growing demands for remote monitoring of these signals from outside the river channel, geophysical seismic-based techniques are increasingly adopted to monitor rivers' EP.

For this remote monitoring, two types of seismic-based geophysical techniques are broadly emerging where the generated seismic-based (GSb) and ambient noise-based (ANb) activities are measured. The seismic signals emitted by river dynamics can be monitored by non-invasive, cost-effective, long-term, and continuous methods with broad applications [12]. Many case histories have been documented in the literature where seismic signals have been used to understand fluvial dynamics [12,24]. Significant efforts have been made to quantify the spectral signature of bedload transportation; however, it has been found that seismic power at low frequency is primarily generated by water discharges rather than bedload transportation [12,25,26]. A theoretical model of PSD was calculated from the Rayleigh waves generated by saltating the bedload particles by [27]. Another seismic activity produced by the turbulent river flow-based theoretical model was proposed by [24]; it contributes to SPD variations in response to the seasonal hysteresis magnitude variations. Similar challenges in the investigation of river flow and hysteresis have been reported in many other studies

 doi:10.20944/preprints202209.0447.v1

[7,12,25,26,28]. These findings support the use of seismic for the high-resolution monitoring of river bedload and other flow attributes [23]. From the previous studies, it can be concluded that for larger fluvial systems, high frequency (> 15 Hz) power excitation is created by high levels of bedload transportation [12,23,29]. In contrast, turbulent flow and discharge modulate lower frequency seismic power (between ~1-10 Hz) [12,28–30].

Contrary, in ANb, the river-sponsored variations in the ambient noise wavefield are induced because of the impacts of the bedload on the riverbed and banks, flow noise generated by the water turbulence, and in response to the acoustic waves generated by the interaction of water and atmosphere [7,31–33]. Monitoring of such river-generated noise is consistently reported in hydrologic studies [33]. ANb monitoring techniques can provide high temporal and spatial resolutions of the landscapes, and their demands are increasing in bedload monitoring because of their low cost and non-invasiveness [23]. In the past decades, an increasing number of contributions have been developed using the variations in ambient noise as the base of the study of the river flow system [25,29,34–36]. It was also found that the river discharge vs noise power followed a seasonal hysteresis trend consistent with the regional sediment transport rates in the river [37]. Additionally, the weak spots along the river terrace can be attributed to the presence of coarse sediments, less compacted sites, soil thickness, and bedrock topography and the objectives can be achieved by GPR application [38–42]. Overall, soil compaction affects soil dielectric constant and GPR EM signals, as reported in previous studies [43].

With the effect of climate change, intermittent and ephemeral systems are expected to become increasingly common globally. However, these systems are understudied compared to perennial stream flows. They are of particular concern as they present a unique connection point at the terrestrial-aquatic interface, promoting soil erosion and landslide triggering. Moreover, complex spatial and temporal variations in hydrologic connectivity in non-perennial systems often require a unique interdisciplinary approach to advance the understanding of their function and response to global change. However, the seismic fluvial dynamic studies were mainly carried out on large rivers while there are very few of them considered small streams for monitoring.

The present study considered an intermittent stream for the analysis that generates small seismic energies related to the sediments and water flows during rainy days in the Federal District of Brazil for the first time. In the first stage, an attempt has been made for the non-invasive detection of weak spots, susceptible to erosion and landslide. Afterwards, the contribution is focused on analyzing how the variations of water discharge in a small river can be observed and monitored using ambient noise analysis. We applied a new monitoring technique that calculates the displacement RMS amplitudes, PSD, spectrograms, and HVSR curves of ambient noise recorded during dry and rainy days. Additionally, HV peak attributes (i.e., amplitude, width, and trough), their changes and relation with different meteorological factors are included in the analysis. Furthermore, GPR data were acquired, and attribute analysis was adopted for the subsurface layering based on geology (soil, boulder, bedrock) and degree of compaction (less compacted, more susceptible to erosion). The study offers insight into the approach applied, which can benefit the broader scientific community involved in seasonal soil losses.

2. Material and Method

2.1. Study site description

Preprints (www.preprints.org) | NOT PEER-REVIEWED | Posted: 28 September 2022 doi:10.20944/preprints202209.0447.v1

The Ribeirão Contagem watershed is extended over 146 km² in the northern part of the Federal District of Brazil in the Sobradinho administrative unit (Figure 1). The study area has a translational landslide whose dynamism is controlled by river erosion [44]. There are alluvial and colluvial materials weathered from the bedrock of the Paranoá group, though bedrock exposures within the channel itself are rare. Most of the Contagem catchment is located on a large erosion complex, where highly active hill slopes supply to channel during summer rainfalls [45]. The Maranhão river is the main tributary of the watershed that flows in the north and northeast directions. The drainage and channel densities of the watershed are 5.7 and 32.9 channels/km², respectively. The climate in the area is semi-humid tropical with a rainy summer and dry winter. The mean annual precipitation in the area is 1,442.5 mm.

The soil analysis included granulometry, and geotechnical tests were performed on the samples collected with an auger and from trenches [47]. As a result, six types of soils are identified in the Contagem basin, including deep and reddish oxisols on the hilltops, shallow inceptisols on the hillslopes, and ultisols because of the presence of clayey carbonate-rich rocks on valleys and plinthic oxisols on the border of hilltops. The erodibility (K factor) is larger for plinthic oxisols than the oxisols and ultissols, having an average value of 0.005790 ton.ha.h.MJ-1.ha-1.mm-1 and 0.004490 ton.ha.h.MJ1.ha-1.mm-1, respectively. The clayey soils in steep hillslopes (from 20° upper to 35° in hills and valleys) can control various linear erosional features such as gullies and landslides e.g., creeps and translational rotational movements. A significant proportion of these erosive features is found in inceptsoil in clay-rich rocks. About 63% of these features occur in close proximity to the river (~20 m), highlighting the active role of hydrological processes in erosion [47].

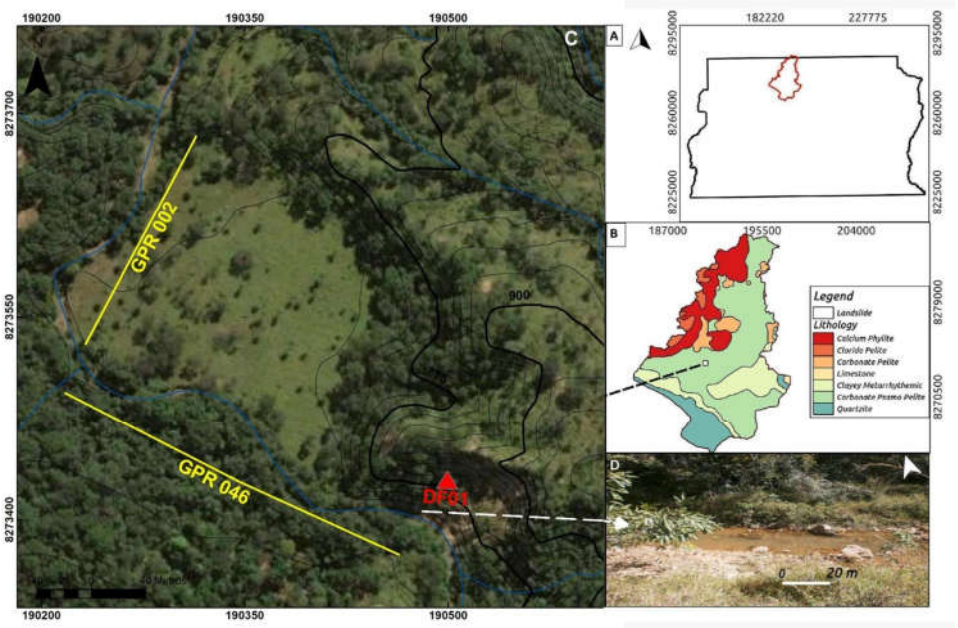

Figure 1. a) Geographic location of Ribeirão Contagem watershed on Federal District map, b) litho-technical units of the watershed c) red dashed ellipse is the Sobradinho

 doi:10.20944/preprints202209.0447.v1

landslide boundary and triangle is the position of seismometer [46] and D) the photograph of river floodplain in the dry season.

The Sobradinho Unit of Votorantim Cimentos Brazil is located in the Ribeirão Contagem Basin, where low-grade metamorphic sediments of the Paranoá and Canastra groups occur. The area is dominated by pelitic rocks such as gray slates and clayey metasiltites. The thickness of the unit varies between 120m and 150m, and the rocks that make up this unit were strongly influenced by the paleogeography of the bottom, marking the end of the deposition of the Paranoá Basin. Due to the composition of this unit, the primary minerals, when in contact with water or subjected to atmospheric conditions, are quickly weathered. The riverbank shows the connection between the colluvial-alluvial material and the alluvial material. The latter has a lateral continuity that varies between ~30 m and ~100 m long from the drainage bed [48]. In the drainage bed, it was possible to observe that the finer-grained alluvial material (with well-selected grains, secondary minerals and low humidity) was superimposed on the colluvial material with poorly selected grains (varying from medium sand to gravel with decimetric boulders), composed of quartz with a high moisture content due to shallow water table. In general, the deposits in the Ribeirão Contagem channel are distributed as follows: soil masses moved by recent rotational landslides; river sediments deposited in recent river bars; sediments deposited in an alluvial fan; colluvial sediments; and alluvial sediments.

Figure 2. a) The former terraces eroding sites (b) photographs of various sizes of sediments from clay to pebbles and boulders in the riverbed, showing the transport capacity in river floods (c) the sediment sequence in terraces show clayey levels and on top with a clast supported layer on the base, showing events of high energy where recurrent (d) sites of undercutting of steep slopes inducing landslides by the river.

Preprints (www.preprints.org) | NOT PEER-REVIEWED | Posted: 28 September 2022 doi:10.20944/preprints202209.0447.v1

[45] proposed a classification for estimating erosive potential (EP) based on hydrological units, slopes, and forms. Three classes were found in the Contagem basin as low, medium, and high erosive potential. Concave hillslopes higher than 10° were classified as high potential due to subsurface flux and clayey material concentration. While on convex slopes, the critical to a movement was taken as 35°. The map showed the major proportion of known mass movements wherein high potential. So, the fluvial valleys and their steep hillslopes are dynamic areas composed of alluvium in the bottom, colluvium in the low and middle parts of the high slopes, shallow inceptsols in the elevated portion of the hillslopes, and oxisols in the hilltops. The concave hillslopes have a critical angle of up to 10°, being the most important trigger of rotational landslides on the border of deep valleys [49].

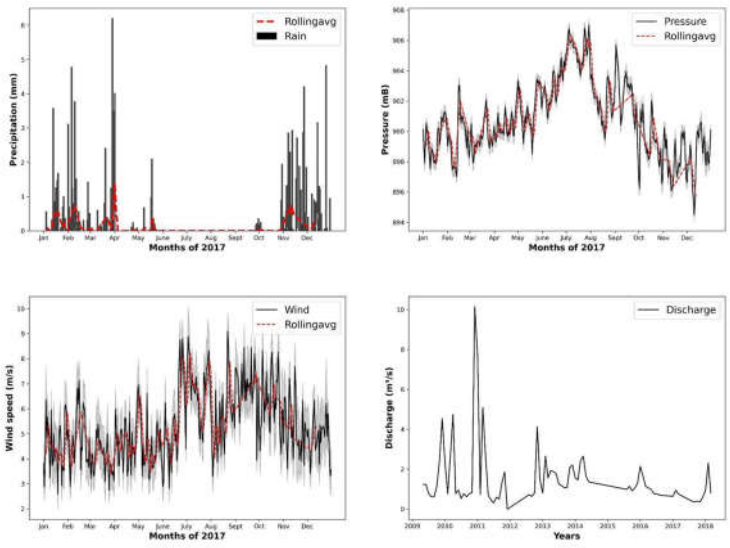

Figure 3. (a) Rainfall, (b) pressure, (c) wind speed and (d) river flow plots of the area.

2.2. Data Acquisition and Processing

2.2.1. Seismic Ambient Noise

For hydrodynamic analysis of the river, one Sorcel L-4A-3D short period seismometer having a natural frequency response of 2 Hz was installed at the bank of the river at the '*Rua do Matto'* locality (Figure 1). The continuous data for the seasonal impact evaluation was divided into two acquisition campaigns (1) dry from Julian day 101 to 105 of 2017 and (2) rainy period from Julian day 344 to 350 of 2017. The records were performed in a continuous mode and at a sampling rate of 250 samples per second with a DAS-130 RefTEK data logger. The raw data were corrected for the instrument response and converted to velocity units. A dataless file was generated using the OBSPY clone function, providing details about the sensor and datalogger used. The signals were demeaned, deterrented and tapered as initial processing.

Commented [HSR1]: Añadir algo sobre la normalización difusa

Commented [HSR2]: Each time window was energy-normalized according to the criterion proposed by S.nchez-Sesma et al. (2011) so as to follow more closely the diffuse approach under which the MHVSR inversions were eventually done.

 doi:10.20944/preprints202209.0447.v1

In the present study, the ambient noise wavefields of dry and rainy days were compared. This comparison was conducted by applying spectral analysis of the ambient noise recorded two times, including power spectral density estimation, time-frequency analysis by spectrogram, and possible quantification effects on the site response by HVSR. After spectral analysis, the displacement RMS of ambient noise of two-time series was also calculated using a widely adopted approach [50]. Details of this processing are provided below.

a) The fast Fourier transform (FFT) of each component is applied to check the response of fluvial mechanisms under the same geological conditions on the same station. In this way, the decomposition of the signal into a discrete spectrum is achieved. The waveform of dry and flooding conditions is selected consisting of ground motion records of N-S, E-W and Z components. "The steps include (i) subdivision of data into smaller windows of time length 50-60 s each with 10% overlap, (ii) each window is 5% cosine tapered and transformed into Fourier domain, and (iii) each spectrum smoothed prior to the calculation of spectrum for a bandwidth coefficient 40, as the raw signal contained unusual spikes [51,52]".

b) The amplitude spectrum is obtained by applying a further transform to the FFT. Power is obtained as a square of the amplitude spectrum. PSDs are gathered by binning periods and powers. These power-period bins are normalized to obtain the probabilistic power spectral density (PPSD). The PSD and its aggregation provide ambient noise energy (power) variations, so the signal strength and distribution is a function of frequency [33,52]. For the validation of spectral analysis, PSD is plotted as functions of rainfall, wind speed, and pressure from the nearby meteorological station. These data are useful in correlating the variation of amplitudes in seismic noise with the sudden changes brought by the rainfall, wind speed and pressure. These meteorological data are divided into ranges and the changes in PSD are observed accordingly.

c) As the seismic energy of a signal is proportional to the square of its amplitude; therefore, the root means square (RMS) analysis of a continuous record provides another way of highlighting the variations of seismic signals with time [53]. Displacement RMS of ambient noise records is calculated using a widely adopted methodology in "COVID Seismology" [50]. It first calculates, the PSD based on which the RMS Displacement derived. To access changes in RMS during hours of the day clock plots are drawn at frequency bands of interest. In order to reduce the high energy ambient noise spikes, a time window of 0.1-7.0 hours is chosen.

Preprints (www.preprints.org) | NOT PEER-REVIEWED | Posted: 28 September 2022 doi:10.20944/preprints202209.0447.v1

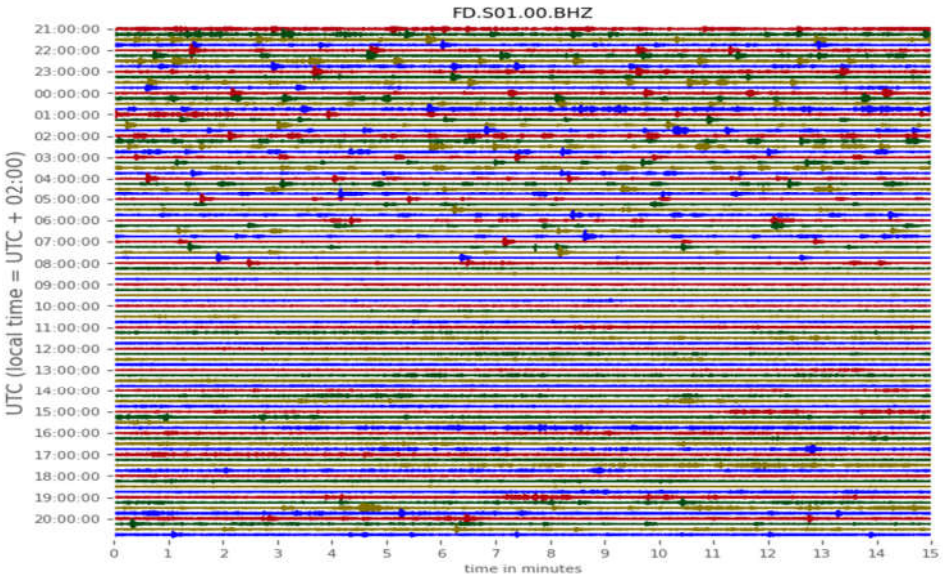

Figure 5. Seismograms recorded during rainy days. Periods of rainfall and river flow can be clearly seen on the plot.

Similarly, to validate RMS results, change-point analysis (CPA), an approach for detecting the numerical value of change in two-time series, was adopted [54]. There are few case studies on the application of CPA in seismology as ambient noise interferometry [55], landslide monitoring [56], and seismic monitoring of COVID-19 [54]. An open-access python rupture library was used for the analysis [57]. We choose an algorithm called Pruned Exact Linear Time (Pelt), adopting a radial basis function model. It works on the assumption that the change-point is unknown and only a penalty parameter is required for the prediction. The choice of penalty is based on the iteration of a set of plenty values. We evaluated the precision and recall metrics for each segmentation for each value. The penalty value chosen was the one that optimized the precision-recall trade-off. This way, the change-point is detected as a function of larger cost function intervals. In this study, we used the RBF cost function, a non-parametric approach based on a Gaussian kernel estimation. It can detect distribution changes rather than shifts in standard statistical measures, such as mean, mode, etc. A detailed explanation of the CPA approach and its application is explained by [54,58].

iii) Time-frequency spectrograms are calculated using obspy (a python library) inbuilt functions, which are expressed in units of energy as dB/(m^2/s^4) over different frequencies.

iv) Changes in local site response can be an important contributor to soil erosion and landslide because detached soil blocks along the bank of the river have their natural period and are excited by the changes in Vs accordingly [44]. Therefore, following [29,34], we applied the HVSR method [59] to the three-component ambient noise records, which provide an ideal scenario for the estimation of site response due to changes in river flow. HVSR provides the response fre-

 doi:10.20944/preprints202209.0447.v1

quency of the loose sedimentary layer over the bedrock if there lies a considerable impedance contrast between them. Using this method, the natural period and the depth of the sedimentary layer are found using equation 1. The FFT of the vertical and horizontal ground motions is calculated after applying an energy normalization on each window following the diffuse approach for the HVSR methodology proposed by [60]. The spectra of both horizontal components are averaged following the vector summation described by [61] and divided by the spectral of the vertical component. In the end, results are smoothened by applying a smooth mean halfwidth 40, and results are plotted. More details about this process are provided elsewhere[62]. Water infiltration and accumulation within unstable compartments may play a fundamental role in site stability. If the unstable compartment is susceptible to water retention, an increase in water content causes an increase in mass (M) and density (ϱ). A decrease in both contact and bulk shear modulus (Gb) is simultaneously expected due to water seepage. A reduction in f1 and a negative dV/V are then expected. Lowering the water table and drying of the material generate the opposite effect [63]

$$f_r = \frac{V_s}{4Z} \quad (1)$$

where Z is the depth, fr is the natural frequency, and Vs is the shear wave velocity.

2.2.2. Ground Penetrating Radar

The dielectric constant of the soil and the degree of its compaction (bulk density/penetration resistance) are somehow related, as documented in the literature [43]. This relationship can be utilized in fluvial seismology for the stratification of soil based on the degree of compaction as loose or unconsolidated soil susceptible to erosion and possible related hazards such as bank erosion. This can also change the river dynamics by increasing the amount of sediment loads and water viscosity, which impacts the seismic (both ANb and ESb).

In this regard, two GPR profiles of 180 m and 360 m long were taken along with the riverbank during dry days using a georadar device GPR GSSI SIR 3000 (Geophysical Services Systems, Nashua, NH, USA), with 400 MHz antenna, control unity, and rugged survey car. The authors used the GPR attributes (i.e., coherence, average amplitude and average energy) for the detailed stratigraphy of the river floodplain as well as marks the degree of compaction (weak spots) of different superficial material types and their susceptibility is discussed in terms of their erodibility.

We used Reflex-win software, version 9.0.5, to do GPR data processing which included: i) static correction for the time zero setting; ii) The "energy decay" module was used to compensate for the signal decay; iii) applying the "background removal" module to suppress or remove the coherent noise or stationary wave noise; iv) 1D type bandpass frequency filtering for removal of high and low-frequency random noise, cutting intervals were set subjectively according to the frequency spectrums of some traces; v) The "running average" module was applied to do data smoothing, the average traces was set as three. After the 5th step, the average amplitude attribute, average energy attribute, and coherence attributes were extracted using the C Language we coded. Finally, the attributes were displayed by the Reflex-win software. The average amplitude attribute is extracted from traditional GPR data by calculating the average of all positive values within a fixed time window, while negative amplitudes are discarded.

 doi:10.20944/preprints202209.0447.v1

In the next stage, the coherence attributes that measure waveform similarity of neighboring traces are calculated to interpret the features of the river floodplain. There are numerous applications of coherence in GPR signal processing [64], after its first use for seismic signals by [65] and first applied to GPR data by [66]. This method achieves coherence using a classical mutual correlation algorithm with 0 and 1 values, and results can be applied to determine valid and invalid signal regions along the GPR profile. Details are provided by [64]. In the end, the coherence image is color scaled as white high and black low values. The boundary of these two signal classes (valid and invalid) is interpreted as a lithological boundary or maximum penetrating depth limit. Valid signals are reflection or echo waves that can be attributed to stratigraphy while invalid signals are the random noise generated by the radar system itself [67].

3. Overview of the findings

3.1. Spectral analysis of seismic ambient noise recordings

PSDs

As described earlier, the spectral analysis includes PSDs, and spectrograms of two ambient noise time series recorded during dry and flooding days. Additionally, the PSDs plotted as a function of wind speed and rainfall. The possible imprints of rainfall on the ambient noise may include the noise because of rainfall drop, river discharge, and properties of sediment loads and check on the urban activities in hours of rain. The details of the findings and discussion are documented below.

PSD as a function of rainfall, wind speed, and pressure are plotted to delineate the effects of these meteorological factors on the power of noise at different frequencies. The wind speed in the considered time is divided into two ranges (Figure 6a). Discharge effects on PSD are clearly seen on horizontal and vertical components. The PSD at low frequency is found unaffected by the wind speed at all considered ranges. However, both time series are directly related at high frequency i.e. PSD is higher at high wind speed and vice versa. Similarly, the rainfall amount during rainy days is divided into two ranges: 0.00-2.47 and 2.47-4.93 mm. Then PSD is plotted as a function of these ranges. It is interesting to note that similar to wind speed, the high rainfall affects the ambient noise PSD at higher frequencies (Figure 7b). The spectral peaks remained with some change in energies the same on all PSD plots.

On PSD plots, the identification of river flow and its sediment loads are discussed in terms of variations in power and peak shifting [68]. These variations are assumed to be excited by the discharge and other related phenomena on rainy days. The changes can also be seen on low-frequency power; this may be associated with the flow considerations of flood-induced changes in the riverbanks' roughness [23]. The peaks at higher-frequency in rainy days (Figure 6d) are associated with variations in the ambient noise wavefields brought by river-related phenomena and effects of other resonant structures such as landslides, local stratigraphy and the other riverine resonant structures related to the deposition of sediments in the floodplain. It may be associated with the same propagating source in the river floods, as explained by [69]. Another possible explanation for these peaks could be the sudden destabilization of debris deposits on slopes and cliffs, which usually result from mass wasting [4].

Preprints (www.preprints.org) | NOT PEER-REVIEWED | Posted: 28 September 2022 doi:10.20944/preprints202209.0447.v1

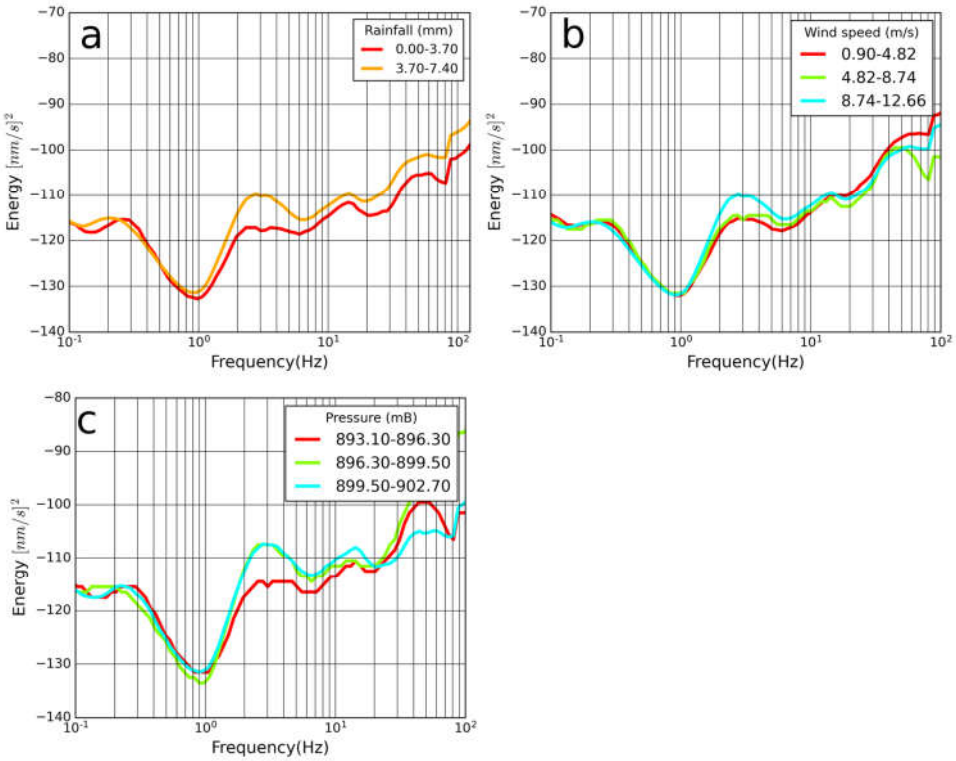

Figure 6. PSD as a function of a) rainfall, b) wind speed, and c) pressure during rainy days at the Z-component of the rainy record.

Figure 6a shows that with the increase in rainfall amount, there is a decrease in PSD at a broad frequency range. The possible explanation for this reduction in noise energy is the attenuation of energies in the soil with a high degree of saturation. There is also a reduction in seismic velocities, especially the shear wave velocity. Wind speed has different effects on the noise energy in dry conditions; as the wind speed rises there is an increase in PSD at a high frequency (2–20 Hz) while the lower frequency remains unaffected (Figure 6b). At a frequency range from 20-100 Hz, this trend does not hold. A similar trend of rising wind speed-increasing PSD during rainy days can be seen in Figure 6b. The fluvial effects on different frequency bands are documented in previous studies as 15–45 Hz [12], 5–15 Hz by [7], 10-30 Hz by [70] and ~0.1–45 Hz by [29]. The debris flow signature at 5-10 Hz frequency band was observed by [13].

Spectograms

The short period spectrograms are shown in Figure 7, which present four different frequency bands (continuous or discontinuous). The spectrograms of two times show low-frequency ambient noise, query blats, and high-frequency noise. The significant energies induced by the river flow below 10 Hz and be-

 doi:10.20944/preprints202209.0447.v1

tween 10-60 Hz can also be seen in Figure 7. These are combined effects of rainfall, river flow, and sediment loads. The sedimentary signals can be seen in Figure 7 as high-frequency events. The frequency band below 2 Hz is the instrumental noise; therefore, it was not possible to see the effects of high wind speed at low frequency. The other high-energy noise band is 2-12 Hz which can be seen on both dry and rainy plots to mark the effects of cultural noise. It also shows a diurnal pattern, another attribute that confirms the presence of cultural noise. The higher frequency band, 20–50 Hz is only prominent on rainy days, showing river-related processes. It is interesting to note that the quarry blast from the nearby mining can be observed on both spectrograms. The spectrograms of dry days don't show any energies at the frequency band where river influence emerged during rainy days. The quiet periods associated with lunch break hours (12-14) at frequencies below 10 Hz can be seen as small windows during rainy days. In literature, the river flow has been observed over different frequency ranges, which depend on the conditions of the river (discharge amount, roughness of river bed) and its site (soil conditions). [71] reported streamflow and sediment transportation the frequency ranges as ~1–20 Hz and ~15–100 Hz, respectively.

Preprints (www.preprints.org) | NOT PEER-REVIEWED | Posted: 28 September 2022 doi:10.20944/preprints202209.0447.v1

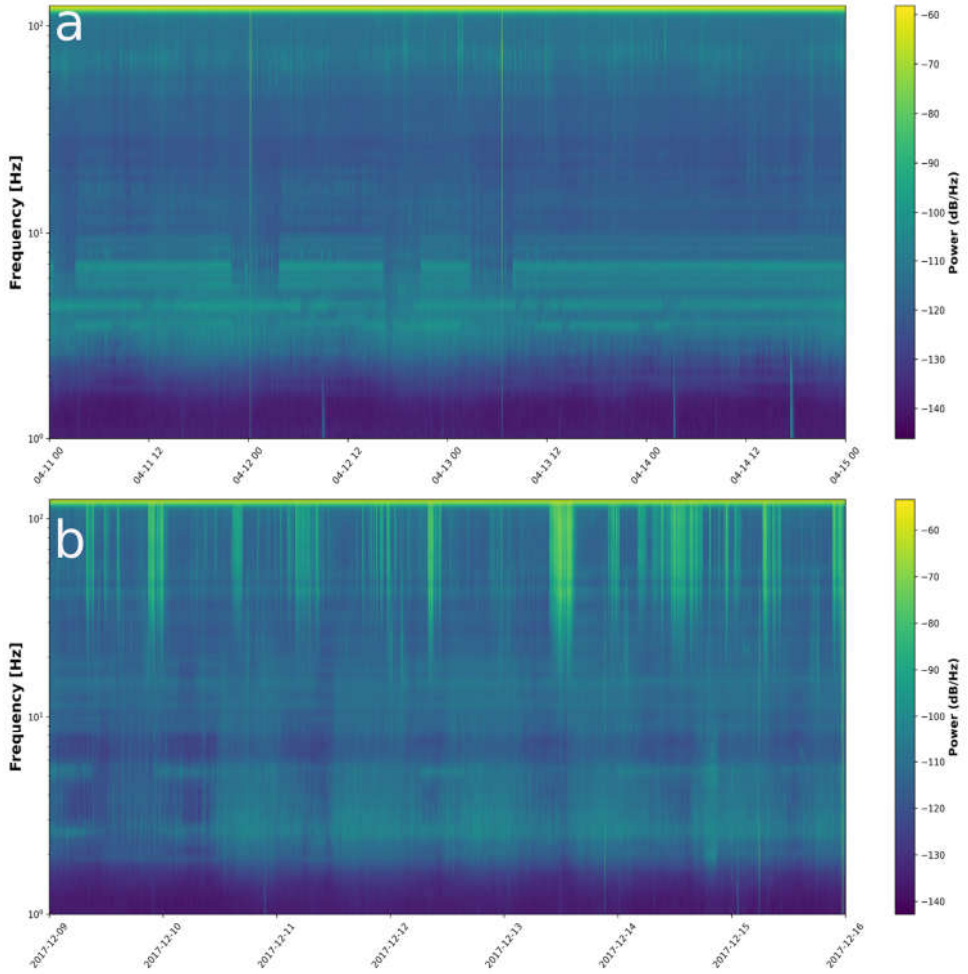

Figure 7. Spectrograms a) dry and b) rainy.

RMS amplitude and energy release

The ambient noise velocity RMS shows variations with hours of the day at different frequencies (2-5 Hz, 30-40 Hz, 50-70 Hz and 70-125 Hz) (Figure 8). It shows stability in ambient noise levels at low frequencies for both the considered time scales. At frequency band of 30-40 Hz and 50-70 Hz, a decrease in RMS values are observed in the rainy days possible associated with break in anthropogenic activities because of rainfall. At frequency range of 2-5 Hz and 70-125Hz an increase in RMS is found. These are the possible frequency ranges where the combined effects (solid-fluid mixture) can be seen. However, the diurnal patterns can be seen in both series at higher frequencies. This may be associated with human activities and the influence of floods in the river at different fre-

Preprints (www.preprints.org) | NOT PEER-REVIEWED | Posted: 28 September 2022 doi:10.20944/preprints202209.0447.v1

quencies; however, as the river is small enough, the influences are less prominent on RMS plots. Under these limited data availability conditions, it is difficult to separate the urban noise and noise generated by the river.

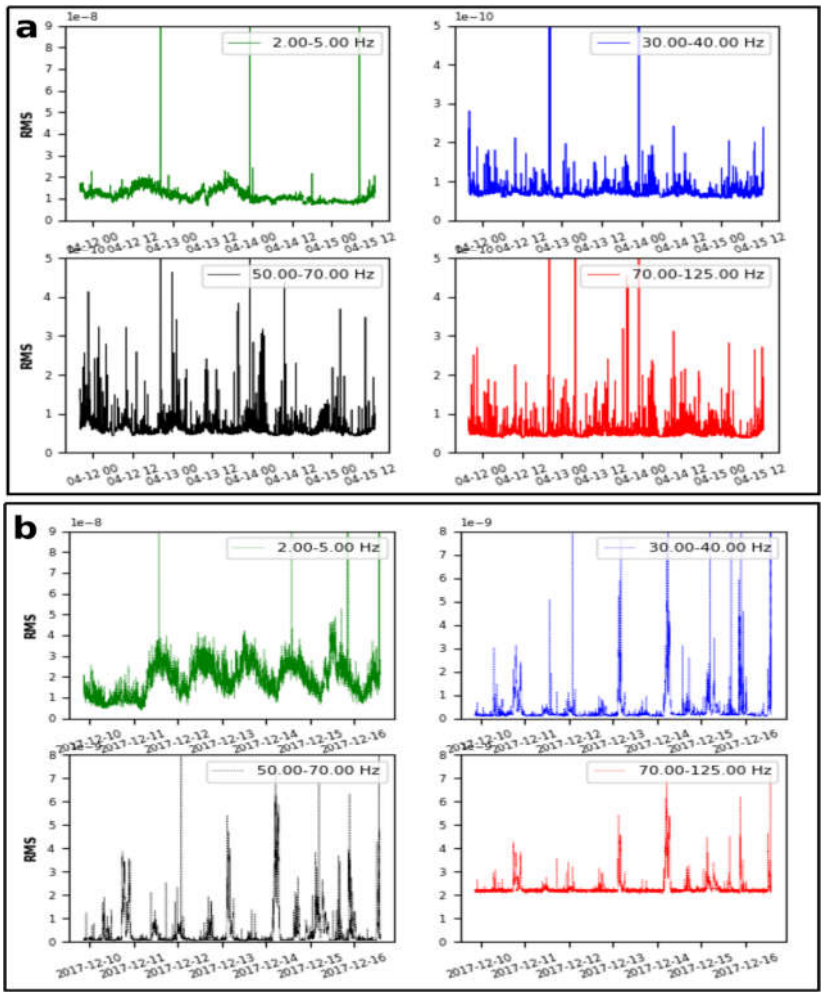

Figure 8. Displacement RMS amplitude of the ambient noise time-series average noise at 6h-16h hours of the day filtered at chosen frequency ranges (2-5 Hz, 30-40 Hz, 50-70 Hz and 70-125 Hz), a) dry and b) rainy days.

Change Point Analysis

Each changing point represents a change in the underlying distribution of the series. The correspondence between wind speed and seismic energy change points demonstrates that both phenomena are correlated somehow. In other words there is an increase in ambient noise RMS with the wind speed and vice versa (Figure 9). The wind can have possible indirect effects by coupling with structures and vegetation on the ground as we buried the seismometer, so the

Preprints (www.preprints.org) | NOT PEER-REVIEWED | Posted: 28 September 2022 doi:10.20944/preprints202209.0447.v1

direct impact of winds is negligible. These effects have also been highlighted in the literature. [72], observed the effects of wind speed on seismic records (HV curves), the ambient noise records and wind speed found well correlated on the Campo de Dalías basin in Spain. There is another study where the effects of windmills have been observed on ambient noise records by [73].

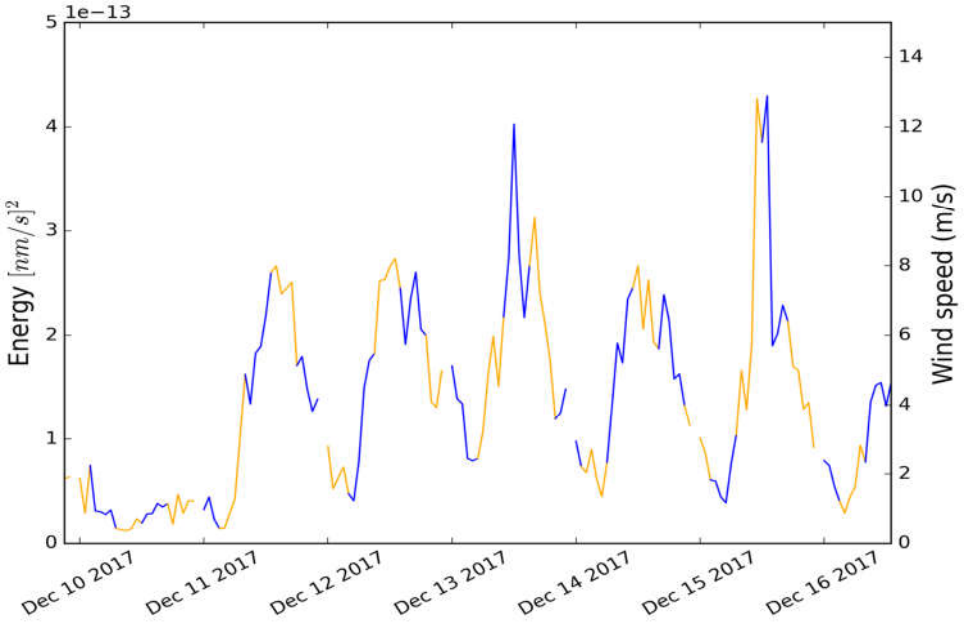

Figure 9. The change of color at each time series represents a change-point automatically detected by a CPA algorithm.

HVSR curves

The HVSR curves obtained for the studied periods, rainy and dry periods, are characterized both by a condition of multiple-peak (Figure 10a). The fundamental HVSR peak identified by [44] as the contact between the low-velocity soft deposits and the Paranoá bedrock is also observed during both periods at 1.3 Hz. Moreover, the secondary peaks attributed to the landslide surface observed by [44] are also identified during the dry season at 4 and 9 Hz showing both significant HVSR amplitudes [74]. This behavior agrees with the findings by [44] for these secondary peaks, which tend to decrease in amplitude or totally disappear during rainy days. On the other hand, the double-peak found above 20 Hz is present in both periods (Figure 10b), and it seems to slightly shift the frequency positions on average of each individual peak as well as to vary the HVSR amplitude when comparing both periods.

In order to compare the differences between the two periods studied Figure 11 gathers the HVSR variations, in terms of frequency and amplitude, for the two persistent peaks observed: the fundamental one at 1.3 Hz and the higher double peak between 20 and 100 Hz. During the rainy period a wider margin of variation is experienced in the two frequency bands, revealing so a period of higher instability in the HVSR curves. Regarding frequency position, the three peaks shift on average to a lower position during the rainy period (Figure 11).

 doi:10.20944/preprints202209.0447.v1

Such observation agrees with the findings by [75], which revealed that the drops in f_0 coincide with sharp increases in water content. This is coherent with the overall soil moisture increasing expected during such a period of heavy rainfalls in the study area. Looking at the daily variations it is observed how a semi-diurnal modulation on the HVSR amplitude exists for the highest secondary peaks, at 40 and 60 Hz, that is kept in both periods (Figure 12). On the contrary, the amplitude variations of the fundamental peak have a daily modulation which loses clarity during the rainy period (Figure 12). While this daily modulation can be related to the well-known pattern of the cultural noise, the semi-diurnal behavior observed in the amplitude modulations of the highest peaks could show a tidal modulation likely induced by the river flow. This fact would support the hypothesis of the river origin behind these two peaks.

Figure 10. a) Averaged HVSR curves of dry (green curve) and rainy days (red curve). b) Zoom to the higher HVSR peaks found between 20 and 100 Hz.

Furthermore, when observing the frequency changes on a daily basis during the two periods (Figure 12), there is no evidence of daily modulations on any of the three HVSR peaks investigated. Comparison with atmospheric data does not show any evidence of a correlation between the non-periodic HVSR frequency fluctuations observed (Figure 12) and the windspeed and atmospheric pressure series for the two periods studied. We assume that they might have been excited by the river discharge and other related fluvial source mechanisms that can be delineated by detailed seismic studies together with UAV monitoring of the river. According to [76], the frequency signature is a function of turbulence, velocity, viscosity, and density, collectively called solid-fluid mixture. This relationship has also been documented elsewhere [77]. If the flow velocity increases, the signal will emerge as low frequency while the viscosity damps the high-frequency signatures [78]. The other factors that affect the frequency spectra by impacting the ground vibrations are the properties of the river bed (geometry, composition, and wetted perimeter) [79]. There is an increase in the frequency of the seismic signal because of the smoothness and softness of bedrock as compared to gravelly or fine sediment composed and dense bedrock, as observed by [80]. Natural period as a function of changes in Vs can be a possible indicator of loose sediments subjected to detachment in response to EP of the river. The gravel bars in the river floodplain have their natural period and are a source of possible resonance peaks at the HVSR curve. In this way, the river bank's compaction and material type can be linked with sediment quantification through natural frequency estimation. These similar features have been delineated based on subsurface stratification achieved by georadar; hence the results are comparable.

Preprints (www.preprints.org) | NOT PEER-REVIEWED | Posted: 28 September 2022 doi:10.20944/preprints202209.0447.v1

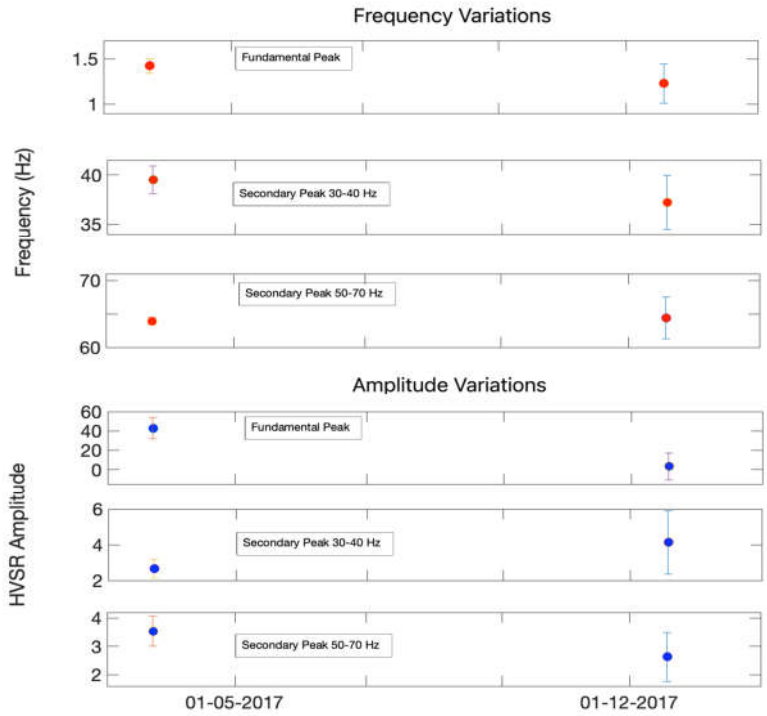

Figure 11. Averaged HVSR variations for the dry (April 2017) and rainy period (December 2017) measured for the fundamental and secondary peaks observed. Error bars show the standard deviation.

Figure 12. HVSR amplitude-variations sampled hourly for the a) fundamental and higher HVSR peaks at b) 40 Hz and c) 60 Hz for dry (April 2017) and rainy period (December 2017).

Figure 13. HVSR frequency-variations sampled hourly for the a) fundamental and higher HVSR peaks at b) 40 Hz and c) 60 Hz for dry (April 2017) and rainy period (December 2017).

3.2. Site characterization by GPR

The GPR coherence attribute provides additional evidence on the subsurface characterization of the stream bed in the floodplain. Boulders, pebbles, and compacted soil have higher coherence values and more reflection interfaces, whereas unconsolidated soil or erodible soil shows lower coherence values and low reflection interfaces. These material interferences are also delineated using coherence attributes where a clear boundary between the valid and invalid signals is found, which is associated with the bedrock interface. We used the "manual pick" mode of Reflexw software to plot the boundary according to the information reflected by the coherence attributes (see Figure 14). GPR images are naturally divided into valid and invalid signal regions and the green line is also shown in other GPR images (Figures 14, 15 & 16). The green line is interpreted

Preprints (www.preprints.org) | NOT PEER-REVIEWED | Posted: 28 September 2022 doi:10.20944/preprints202209.0447.v1

as the boundary of the valid and invalid signal regions. In the valid region of the GPR data profile, the reflection wave signals are dominated. In the invalid region, GPR data can't be used to interpret geological units. There are two possible explanations for marking the depth boundary: electrical conductivity, the signal transmitted by GPR decayed to zero on reaching the depth marked by the green line in Figure 14. Another reason could be the presence of a compacted bedrock interface without a reflector (no flection wave goes back), and GPR can only record random noise signals.

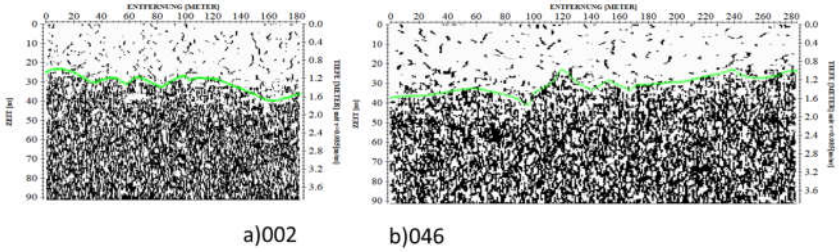

Figure 14. GPR coherence attribute a) profile 046 and b) profile 002. The green line is interpreted as the boundary between valid and invalid signals.

Contrasted with the traditional GPR image, where the boundary is considered the termination position or bottom of a dense, strong amplitude region [81], the coherence attribute can reduce the ambiguity and subjectivity of the boundary interpretation. The black dashed line in Figure 15 marks the different part of the probable boundary interpreted by the traditional method with the boundary (green line) interpreted using the coherence attribute. The traditional interpretation method can probably ignore the weak amplitude signals that contain effective reflection signals, such as the area between the black dashed line and solid green line in Figure 15. The coherence attribute wipes off the amplitude information of signals and only reflects the signal waveforms, which reduces the ambiguities in the boundary interpretation.

We acquired the GPR data in the dry season, so the soil water content and conductivity are lower compared to the rainy season. In this way, the deeper penetration of GPR signals in the soil can be achieved as well as the invalid signal region corresponds to the highly compacted bedrock leading to a reduction in the emergence of the reflection interface. In the valid region, a low coherence value indicates the change in subsurface media or structure, such as presence of rock fragments, pebbles, soil voids, small faults or other related discontinuities. The region corresponding to the high coherence value (white color) presents a higher degree of compaction relative to the corresponding low coherence value (black color) parts in the valid region. Therefore, we consider this position reflected by the black low coherence value in the valid region as the susceptible points to erosion. For instance, soil voids or discontinuity can provide permeable paths where rain water can infiltrate into the subsurface and may cause instability by building pore water pressure [82].

Preprints (www.preprints.org) | NOT PEER-REVIEWED | Posted: 28 September 2022 doi:10.20944/preprints202209.0447.v1

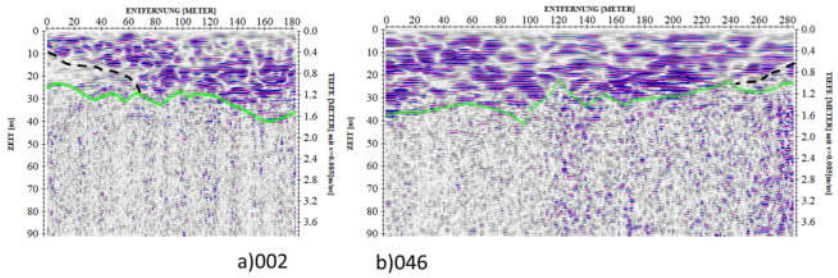

Figure 15. Traditional GPR images a) profile 002and b) profile 046. The solid green and dashed black lines are interpreted by the traditional method and coherence attribute, respectively.

The average energy attribute can be used to delineate the presence and geometry of buried pebbles or boulders to the fact that the interface of rock and soil can reflect high energy waves with significant differences in electrical properties among them. Therefore, the places of high energy value may correspond to the positions of subsurface boulders and information about their sizes can be inferred from the dimensions of the purple color regions on the energy attribute image (Figure 16).

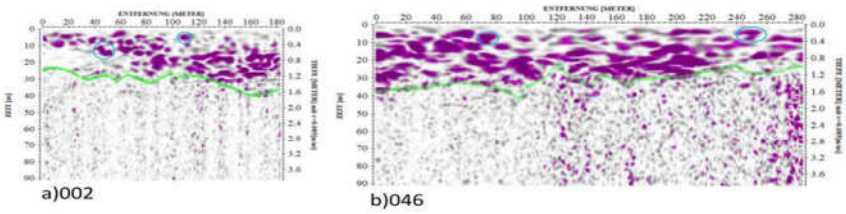

Figure 16. GPR average energy attribute a) profile 002 and b) profile 046. The green line is the boundary of the valid and invalid signal regions. The purple color is high in average energy value, while white and gray are lower values. The blue circles marked out some possible boulders underground.

The traditional GPR images in Figure 16 contain purple and blue colors to display the strong positive and negative signals to observe the stratigraphy featured. Figure 17 clearly reflects that the subsurface layers generally are the distribution characteristics of approximately horizontal deposition. Some tilted deposit layers are also evident in the images, especially in Figure 17a. Only the valid signal region can be applied for the stratigraphy interpretation in the average amplitude attribute (Figure 17). The average amplitude attribute can be more convenient and visual for layer depth interpretation.

 doi:10.20944/preprints202209.0447.v1

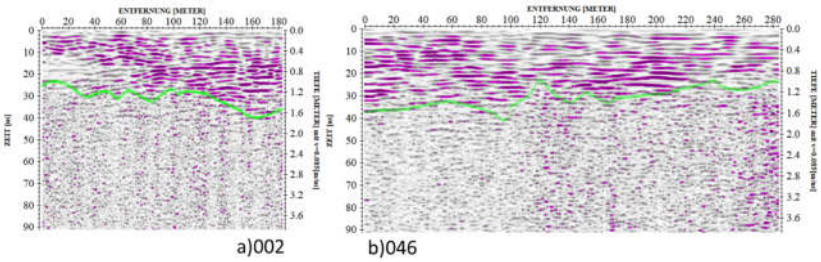

Figure 17. GPR amplitude attribute a) profile 002 and b) profile 046. The green line is the boundary of the valid and invalid signal regions. Purple is high value, and white and gray are low value. .

4. Conclusions

This study presents seismic monitoring and analysis of the river sediment carrying capacity in the *Ribeirão Contagem* watershed (of the Federal district of Brazil) on rainy and dry days. The GPR-based local site conditions and their possible impacts on the erosion and sediments load of the river are discussed. The ambient noise wavefields during dry and rainy days are measured and compared. This comparison was conducted by applying spectral analysis of the ambient noise (recorded two times) including power spectral density estimation, time-frequency analysis by spectrogram, and possible quantification effects on the site response by HVSR curves. Based on the findings, we may conclude the followings:

i) Ambient noise-based analysis showed variations in the PSD on rainy and dry days. An apparent change of spectrogram of rainy days was identified, attributed to rainfall and river dynamics. PSD vs. meteorological agent (rainfall and wind speed) plots showed an apparent increase in PSD during rainy days.

iii) Based on the spectrograms of the rainy days (the signals and their characteristics), it can be suggested that one of the signals dominantly results from bedload transport and the other two from fluid transport processes.

iv) The HVSR plots showed an increase in amplitude starting from 10 Hz. During rainy days, a shift of to low frequency and a semi-diurnal modulation on the higher peaks is observed.

v) Ambient noise RMS plots evidently showed variations in displacement during daytime. The correspondence between wind speed and seismic energy CPA demonstrates that both phenomena are somehow correlated.

vi) GPR average amplitude attribute profiles showed the detailed riverbank and floodplain stratigraphy. It delineates the depth and topography of bedrock. Energy attributes may be used for judging the presence of builders. The coherence attribute can help evaluate the degree of compaction and possible indication to the region as the susceptible points to erosion (weak spots). The invalid region corresponds to a high degree of compaction area in the subsurface because a little reflection surface can reflect waves, and GPR can only record random noise.

Based on the variations and emergence of new typologies on different frequency bands, we assume that they might have been excited by the river discharge and other related fluvial source mechanisms that can be delineated by detailed seismic studies together with UAV monitoring of the river.

Acknowledgments:

Conflicts of Interests: Authors declare no conflict of interests.

Data Availability: Data are available by emailing the corresponding author.

References

1. Somos-Valenzuela, M.A.; Mckinney, D.C.; Byers, A.C.; Rounce, D.R.; Portocarrero, C.; Lamsal, D. Assessing Downstream Flood Impacts Due to a Potential GLOF from Imja Tsho in Nepal. *Hydrol. Earth Syst. Sci* **2015**, *19*, 1401–1412, doi:10.5194/hess-19-1401-2015.
2. Zhang, J.; Zhou, L.; Huang, D. Development of Rill Erosion on Bare Sloping Farmland under Natural Rainfall Conditions. *Environ. Earth Sci.* **2022**, *81*, doi:10.1007/s12665-022-10383-z.
3. Gu, Y.F.; Jin, X.D.; Xiang, R.Z.; Wang, Q.W.; Wang, C.; Yang, S.X. UAV-Based Integrated Multispectral-LiDAR Imaging System and Data Processing. *Sci. China Technol. Sci.* **2020**, *63*, doi:10.1007/s11431-019-1571-0.
4. Chmiel, M.; Godano, M.; Piantini, M.; Brigode, P.; Gimbert, F.; Bakker, M.; Courboulex, F.; Ampuero, J.P.; Rivet, D.; Sladen, A.; et al. Brief Communication: Seismological Analysis of Flood Dynamics and Hydrologically Triggered Earthquake Swarms Associated with Storm Alex. *Nat. Hazards Earth Syst. Sci.* **2022**, *22*, 1541–1558, doi:10.5194/nhess-22-1541-2022.
5. Lawler, D.M. The Measurement of River Bank Erosion and Lateral Channel Change: A Review. *Earth Surf. Process. Landforms* **1993**, *18*, 777–821, doi:10.1002/esp.3290180905.
6. Graf, W.L.; Wohl, E.; Sinha, T.; Sabo, J.L. Sedimentation and Sustainability of Western American Reservoirs. *Water Resour. Res.* **2010**, *46*, doi:10.1029/2009WR008836.
7. Chao, W.A.; Wu, Y.M.; Zhao, L.; Tsai, V.C.; Chen, C.H. Seismologically Determined Bedload Flux during the Typhoon Season. *Sci. Rep.* **2015**, *5*, 1–8, doi:10.1038/srep08261.
8. Giménez, R.; Casalí, J.; Grande, I.; … J.D.-A.W.; 2012, undefined Factors Controlling Sediment Export in a Small Agricultural Watershed in Navarre (Spain). *Elsevier*.
9. David, M.B.; Drinkwater, L.E.; McIsaac, G.F. Sources of Nitrate Yields in the Mississippi River Basin. *J. Environ. Qual.* **2010**, *39*, 1657–1667, doi:10.2134/jeq2010.0115.
10. Oeurng, C.; Sauvage, S.; Sánchez-Pérez, J.M. Dynamics of Suspended Sediment Transport and Yield in a Large Agricultural Catchment, Southwest France. *Earth Surf. Process. Landforms* **2010**, *35*, 1289–1301, doi:10.1002/esp.1971.
11. Araujo, H.A.; Cooper, A.B.; Hassan, M.A.; Venditti, J. Estimating Suspended Sediment Concentrations in Areas with Limited Hydrological Data Using a Mixed-Effects Model. *Hydrol. Process.* **2012**, *26*, 3678–3688, doi:10.1002/hyp.8462.
12. Schmandt, B.; Aster, R.C.; Scherler, D.; Tsai, V.C.; Karlstrom, K. Multiple Fluvial Processes Detected by Riverside Seismic and Infrasound Monitoring of a Controlled Flood in the Grand Canyon. *Geophys. Res. Lett.* **2013**, *40*, 4858–4863, doi:10.1002/grl.50953.
13. Lai, V.H.; Tsai, V.C.; Lamb, M.P.; Ulizio, T.P.; Beer, A.R. The Seismic Signature of Debris Flows: Flow Mechanics and Early Warning at Montecito, California. *Geophys. Res. Lett.* **2018**, *45*, 5528–5535, doi:10.1029/2018GL077683.
14. Marchetti, E.; Walter, F.; Barfucci, G.; Genco, R.; Wenner, M.; Ripepe, M.; McArdell, B.; Price, C. Infrasound Array Analysis of Debris Flow Activity and Implication for Early Warning. *J. Geophys. Res. Earth Surf.* **2019**, *124*, 567–587, doi:10.1029/2018JF004785.
15. Hamza, O.; De Vargas, T.; Boff, F.E.; Hussain, Y.; Sian Davies-Vollum, K. Geohazard Assessment of Landslides in South Brazil: Case Study. *Geotech. Geol. Eng.* **2020**, *38*, doi:10.1007/s10706-019-01054-1.
16. Cunha, E.R. da; Santos, C.A.G.; Silva, R.M. da; Panachuki, E.; de Oliveira, P.T.S.; Oliveira, N. de S.; Falcão, K. dos S. Assessment of Current and Future Land Use/Cover Changes in Soil Erosion in the Rio Da Prata Basin (Brazil). *Sci. Total Environ.* **2022**, *818*, 151811, doi:10.1016/j.scitotenv.2021.151811.
17. Gomes, L.; Simões, S.J.C.; Lennon, E.; Nora, D.; Rodrigues De Sousa-Neto, E.; Forti, M.C.; Pierre, J.; Ometto, H.B. Agricultural Expansion in the Brazilian Cerrado: Increased Soil and Nutrient Losses and Decreased Agricultural Productivity. *mdpi.com*, doi:10.3390/land8010012.
18. Fonseca, M.; … R.U.-E.S.P.; 2022, undefined Rates, Factors, and Tolerances of Water Erosion in the Cerrado Biome (Brazil): A Meta-analysis of Runoff Plot Data. *academia.edu*.
19. Louzada, R.S.; Tavares, A.S. Revista Brasileira de Geomorfologia Monitoramento Da Vazão e Carga Sólida Suspensa Em Eventos Pluviais Na Bacia Do Ribeirão Do Gama/DF Monitoring of Flow and Suspended Solid Load in Rainfall Events in the Ribeirão Do Gama Basin/DF. *rbgeomorfologia.org.br* **2022**, doi:10.20502/rbg.v23i3.2134.
20. Turowski, J.M.; Badoux, A.; Rickenmann, D. Start and End of Bedload Transport in Gravel-Bed Streams. *Geophys. Res. Lett.* **2011**, *38*, doi:10.1029/2010GL046558.
21. Schneider, J.M.; Turowski, J.M.; Rickenmann, D.; Hegglin, R.; Arrigo, S.; Mao, L.; Kirchner, J.W. Scaling Relationships between Bed Load Volumes, Transport Distances, and Stream Power in Steep Mountain Channels. *J. Geophys. Res. Earth Surf.* **2014**, *119*, doi:10.1002/2013JF002874.
22. Wilcock, P.R.; Crowe, J.C. Surface-Based Transport Model for Mixed-Size Sediment. *J. Hydraul. Eng.* **2003**, *129*, doi:10.1061/(asce)0733-9429(2003)129:2(120).
23. Roth, D.L.; Brodsky, E.E.; Finnegan, N.J.; Rickenmann, D.; Turowski, J.M.; Badoux, A. Bed Load Sediment Transport Inferred from Seismic Signals near a River. *Wiley Online Libr.* **2016**, *121*, 725–747, doi:10.1002/2015JF003782.

24. Gimbert, F.; Tsai, V.; Geophysical, M.L.-J. of; 2014, undefined A Physical Model for Seismic Noise Generation by Turbulent Flow in Rivers. *Wiley Online Libr.* **2014**, *119*, 2209–2238, doi:10.1002/2014JF003201.
25. Burtin, A.; Bollinger, L.; Vergne, J.; Cattin, R.; Nábělek, J.L. Spectral Analysis of Seismic Noise Induced by Rivers: A New Tool to Monitor Spatiotemporal Changes in Stream Hydrodynamics. *J. Geophys. Res.* **2008**, *113*, B05301, doi:10.1029/2007JB005034.
26. Barrière, J.; Oth, A.; Hostache, R.; Krein, A. Bed Load Transport Monitoring Using Seismic Observations in a Low-Gradient Rural Gravel Bed Stream. *Geophys. Res. Lett.* **2015**, *42*, 2294–2301, doi:10.1002/2015GL063630.
27. Tsai, V.C.; Minchew, B.; Lamb, M.P.; Ampuero, J.-P. A Physical Model for Seismic Noise Generation from Sediment Transport in Rivers. *Res. Lett* **2012**, *39*, 2404, doi:10.1029/2011GL050255.
28. Burtin, A.; Cattin, R.; Bollinger, L.; Vergne, J.; Steer, P.; Robert, A.; Findling, N.; Tiberi, C. Towards the Hydrologic and Bed Load Monitoring from High-Frequency Seismic Noise in a Braided River: The "Torrent de St Pierre", French Alps. *J. Hydrol.* **2011**, *408*, 43–53, doi:10.1016/j.jhydrol.2011.07.014.
29. Anthony, R.E.; Aster, R.C.; Ryan, S.; Rathburn, S.; Baker, M.G. Measuring Mountain River Discharge Using Seismographs Emplaced Within the Hyporheic Zone. *J. Geophys. Res. Earth Surf.* **2018**, *123*, 210–228, doi:10.1002/2017JF004295.
30. Bartholomaus, T.C.; Amundson, J.M.; Walter, J.I.; O'Neel, S.; West, M.E.; Larsen, C.F. Subglacial Discharge at Tidewater Glaciers Revealed by Seismic Tremor. *Geophys. Res. Lett.* **2015**, *42*, 6391–6398, doi:10.1002/2015GL064590.
31. Bakker, M.; Gimbert, F.; Geay, T.; Misset, C.; Zanker, S.; Recking, A. Field Application and Validation of a Seismic Bedload Transport Model. *J. Geophys. Res. Earth Surf.* **2020**, *125*, e2019JF005416, doi:10.1029/2019JF005416.
32. Lagarde, S.; Dietze, M.; … F.G.-W.R.; 2021, undefined Water Resources Research. *Wiley Online Libr.* **2021**, *57*, doi:10.1029/2020WR028700.
33. Díaz, J.; Ruíz, M.; Crescentini, L.; Amoruso, A.; Gallart, J. Seismic Monitoring of an Alpine Mountain River. *J. Geophys. Res. Solid Earth* **2014**, *119*, 3276–3289, doi:10.1002/2014JB010955.
34. Goodling, P.; Dynamics, V.L.-E.S.; 2018, undefined Seismic Signature of Turbulence during the 2017 Oroville Dam Spillway Erosion Crisis. *esurf.copernicus.org*.
35. Smith, K.; Tape, C. Seismic Noise in Central Alaska and Influences From Rivers, Wind, and Sedimentary Basins. *J. Geophys. Res. Solid Earth* **2019**, *124*, 11678–11704, doi:10.1029/2019JB017695.
36. P.C, S.; Sawazaki, K. River Discharge Prediction for Ungauged Mountainous River Basins during Heavy Rain Events Based on Seismic Noise Data. *Prog. Earth Planet. Sci.* **2021**, *8*, doi:10.1186/s40645-021-00448-1.
37. Gabet, E.; Burbank, D.; … B.P.-S.-E. and P.; 2008, undefined Modern Erosion Rates in the High Himalayas of Nepal. *Elsevier*.
38. Arcone, S.A.; Lawson, D.E.; Delaney, A.J.; Strasser, J.C.; Strasser, J.D. Ground-Penetrating Radar Reflection Profiling of Groundwater and Bedrock in an Area of Discontinuous Permafrost. *Geophysics* **1998**, *63*, 1573–1584, doi:10.1190/1.1444454.
39. Szuch, R.P.; White, J.G.; Vepraskas, M.J.; Doolittle, J.A. Application of Ground Penetrating Radar to Aid Restoration Planning for a Drained Carolina BAY. *Wetlands* 2006, *26*, 205–216.
40. Weihermüller, L.; Huisman, J.; Lambot, S.; … M.H.-J. of; 2007, undefined Mapping the Spatial Variation of Soil Water Content at the Field Scale with Different Ground Penetrating Radar Techniques. *Elsevier*.
41. Fabregat, I.; Gutiérrez, F.; Roqué, C.; … M.Z.-Q.; 2019, undefined Subsidence Mechanisms and Sedimentation in Alluvial Sinkholes Inferred from Trenching and Ground Penetrating Radar (GPR). Implications for Subsidence And. *Elsevier*.
42. Chalikakis, K.; Plagnes, V.; Guerin, R.; Valois, R.; Bosch, F.P. Contribution of Geophysical Methods to Karst-System Exploration: An Overview. *Hydrogeol. J.* **2011**, *19*, 1169–1180, doi:10.1007/s10040-011-0746-x.
43. Wang, P.; Hu, Z.; Zhao, Y.; Geophysics, X.L.-J. of A.; 2016, undefined Experimental Study of Soil Compaction Effects on GPR Signals. *Elsevier*.
44. Hussain, Y.; Cardenas-Soto, M.; Martino, S.; Moreira, C.; Borges, W.; Hamza, O.; Prado, R.; Uagoda, R.; Rodríguez-Rebolledo, J.; Silva, R.C.; et al. Multiple Geophysical Techniques for Investigation and Monitoring of Sobradinho Landslide, Brazil. *Sustain.* **2019**, *11*, doi:10.3390/su11236672.
45. Ferreira, R., Uagoda, R. Morphometric Study of Controls to Erosional Features and Identification of Areas Susceptible to Mass Movement Hazards in the Contagem Watershed, Distrito Federal. *Rev. Espaço e Geogr.* **2015**, *18*, 187:216.
46. Hussain, Y.; Cardenas-Soto, M.; Uagoda, R.; Martino, S.; Rodriguez-Rebolledo, J.; Hamza, O.; Martinez-Carvajal, H. Monitoring of Sobradinho Landslide (Brasília, Brazil) and a Prototype Vertical Slope by Time-Lapse Interferometry. *Brazilian J. Geol.* **2019**, *49*, doi:10.1590/2317-4889201920180085.
47. Braga, Ligier; Raina, Ferreira; Uagoda, R. (PDF) MORPHOMETRIC STUDY OF CONTROLS TO EROSIONAL FEATURES AND IDENTIFICATION OF AREAS SUSCEPTIBLE TO MASS MOVEMENT HAZARDS IN THE CONTAGEM WATERSHED, DISTRITO FEDERAL. *Espaço Geogr.* **2017**, *20*, 99:121.
48. da Silva Nunes, J.G.; Uagoda, R.; Caldeira, D.; Braga, L.M.; Hussain, Y.; Carvajal, H.M. Application of GPR for the Differentiation of Alluvial and Colluvial Materials, Based on Direct Observation in Contagem Valley – Distrito Federal (Brasil). *Rev. Bras. Geomorfol.* **2019**, *20*, 217–238, doi:10.20502/rbg.v20i2.1382.
49. Modesto Braga, L.; Caldeira, D.; Gustavo da Silva Nunes, J.; Hussain, Y.; Martinez Carvajal, H.; Uagoda, R. Caracterização Geomorfológica e Dinâmica Erosivo-Deposicional de Encostas No Vale Fluvial Do Ribeirão

Contagem-DF, Brasil Geomorphological Description and Erosive-Depositional Dynamics of Hillslopes on Ribeirão Contagen Fluvial Valley-DF, Brazil. *revistas.ufrj.br*, doi:10.11137/2018_2_51_65.

50. Lecocq, T.; Hicks, S.P.; van Noten, K.; van Wijk, K.; Koelemeijer, P.; de Plaen, R.S.M.; Massin, F.; Hillers, G.; Anthony, R.E.; Apoloner, M.T.; et al. Global Quieting of High-Frequency Seismic Noise Due to COVID-19 Pandemic Lockdown Measures. *Science (80-.).* **2020**, *369*, 1338–1343, doi:10.1126/science.abd2438.
51. Singh, A.P.; Kumar, M.R.; Pandey, A.; Roy, K.S. Investigation of Spatial and Temporal Variability of Site Response in the Arunachal Himalaya Using Ambient Seismic Noise and Earthquake Waveforms. *Near Surf. Geophys.* **2019**, *17*, 427–445, doi:10.1002/nsg.12053.
52. Pandey, A.P.; Singh, A.P.; Bansal, B.K.; Suresh, G.; Prajapati, S.K. Appraisal of Seismic Noise Scenario at National Seismological Network of India in COVID-19 Lockdown Situation. *Taylor Fr.* **2020**, *11*, 2095–2122, doi:10.1080/19475705.2020.1830187.
53. Falanga, M.; Cusano, P.; Lauro, E. De; Reports, S.P.-S.; 2021, undefined Picking up the Hydrothermal Whisper at Ischia Island in the Covid-19 Lockdown Quiet. *nature.com*.
54. Maciel, S.; Rocha, M.; one, M.S.-P.; 2021, undefined Urban Seismic Monitoring in Brasília, Brazil. *journals.plos.org*.
55. Sánchez-Pastor, P.; Obermann, A.; Schimmel, M. Detecting and Locating Precursory Signals During the 2011 El Hierro, Canary Islands, Submarine Eruption. *Geophys. Res. Lett.* **2018**, *45*, 10,288-10,297, doi:10.1029/2018GL079550.
56. Amorese, D.; Grasso, J.-R.; Garambois, S.; Font, M. Change-Point Analysis of Geophysical Time-Series: Application to Landslide Displacement Rate (Séchilienne Rock Avalanche, France). *Geophys. J. Int.* **2018**, *213*, 1231–1243, doi:10.1093/gji/ggy060.
57. Truong, C.; Oudre, L.; Processing, N.V.-S.; 2020, undefined Selective Review of Offline Change Point Detection Methods. *Elsevier*.
58. Lykou, R.; Tsaklidis, G.; Mechanics, E.P.-P.A.S.; 2020, undefined Change Point Analysis on the Corinth Gulf (Greece) Seismicity. *Elsevier*.
59. Nakamura, Y. Method for Dynamic Characteristics Estimation of Subsurface Using Microtremor on the Ground Surface. *Q. Rep. RTRI (railw. Tech. Res. Institute)* **1989**, *30*.
60. Sánchez-Sesma, F.J.; Rodríguez, M.; Iturrarán-Viveros, U.; Luzón, F.; Campillo, M.; Margerin, L.; García-Jerez, A.; Suarez, M.; Santoyo, M.A.; Rodríguez-Castellanos, A. A Theory for Microtremor H/V Spectral Ratio: Application for a Layered Medium. *Geophys. J. Int.* **2011**, *186*, doi:10.1111/j.1365-246X.2011.05064.x.
61. Albarello, D.; Lunedei, E. Combining Horizontal Ambient Vibration Components for H/V Spectral Ratio Estimates. *Geophys. J. Int.* **2013**, *194*, doi:10.1093/gji/ggt130.
62. Hussain, Y.; Cardenas-Soto, M.; Moreira, C.; Rodriguez-Rebolledo, J.; Hamza, O.; Prado, R.; Martinez-Carvajal, H.; Dou, J. Variation in Rayleigh Wave Ellipticity as a Possible Indicator of Earthflow Mobility: A Case Study of Sobradinho Landslide Compared with Pile Load Testing. *Earth Sci. Res. J.* **2020**, *24*, 141–151, doi:10.15446/esrj.v24n2.81974.
63. Colombero, C.; Jongmans, D.; Fiolleau, S.; Valentin, J.; Baillet, L.; Bièvre, G. Seismic Noise Parameters as Indicators of Reversible Modifications in Slope Stability: A Review. *Surv. Geophys.* 2021, *42*.
64. Gao, Q.; Wang, S.; Peng, T.; Peng, H.; Geomorphology, D.O.-; 2020, undefined Evaluating the Structure Characteristics of Epikarst at a Typical Peak Cluster Depression in Guizhou Plateau Area Using Ground Penetrating Radar Attributes. *Elsevier*.
65. Bahorich, M.; Farmer, S. The Coherence Cube. *Lead. Edge* **1995**.
66. Young, R.A.; Deng, Z.; Marfurt, K.J.; Nissen, S.E. 3-D Dip Filtering and Coherence Applied to GPR Data: A Study. *Lead. Edge* **1997**, *16*, 921, doi:10.1190/1.1437699.
67. Jol, H. *Ground Penetrating Radar Theory and Applications*; 2008;
68. Wenner, M.; Walter, F.; Mcardell, B.; Farinotti, D. *Deciphering Debris-Flow Seismograms at Illgraben, Switzerland*;
69. Piantini, M.; Gimbert, F.; Bellot, H.; Recking, A. Triggering and Propagation of Exogenous Sediment Pulses in Mountain Channels: Insights from Flume Experiments with Seismic Monitoring. *Earth Surf. Dyn.* **2021**, *9*, 1423–1439, doi:10.5194/esurf-9-1423-2021.
70. Schimmel, A.; Hübl, J.; McArdell, B.W.; Walter, F. Automatic Identification of Alpine Mass Movements by a Combination of Seismic and Infrasound Sensors. *Sensors (Switzerland)* **2018**, *18*, doi:10.3390/s18051658.
71. Polvi, L.E.; Dietze, M.; Lotsari, E.; Turowski, J.M.; Lind, L. Seismic Monitoring of a Subarctic River: Seasonal Variations in Hydraulics, Sediment Transport, and Ice Dynamics. *Wiley Online Libr.* **2020**, *125*, doi:10.1029/2019JF005333.
72. Seivane, H.; García-Jerez, A.; Navarro, M.; Molina, L.; Navarro-Martínez, F. On the Use of the Microtremor HVSR for Tracking Velocity Changes: A Case Study in Campo de Dalías Basin (SE Spain). *Geophys. J. Int.* **2022**, *230*, 542–564, doi:10.1093/gji/ggac064.
73. Saccorotti, G.; Piccinini, D.; Cauchie, L.; Fiori, I. Seismic Noise by Wind Farms: A Case Study from the Virgo Gravitational Wave Observatory, Italy. *Bull. Seismol. Soc. Am.* **2011**, *101*, 568–578, doi:10.1785/0120100203.
74. SESAME Guidelines for The Implementation of The H/V Spectral Ratio Technique on Ambient Vibrations-Measurements, Processing and Interpretations, SESAME European Research Project. *SESAME Site Eff. Assess. using Ambient Excit.* **2004**, 1–62.

 doi:10.20944/preprints202209.0447.v1

75. Stevens, N.; FastTIMES, S.J.-; 2022, undefined Capturing the Changing Cryosphere with Seismic Horizontal-Vertical Spectral Ratios. *fasttimesonline.co*.
76. Walsh, B.; Coviello, V.; Capra, L.; Procter, J.; Márquez-Ramirez, V. Insights Into the Internal Dynamics of Natural Lahars From Analysis of 3-Component Broadband Seismic Signals at Volcán de Colima, Mexico. *Front. Earth Sci.* **2020**, *8*, doi:10.3389/feart.2020.542116.
77. Coviello, V.; Arattano, M.; Comiti, F.; Macconi, P.; Marchi, L. Seismic Characterization of Debris Flows: Insights into Energy Radiation and Implications for Warning. *J. Geophys. Res. Earth Surf.* **2019**, *124*, 1440–1463, doi:10.1029/2018JF004683.
78. Huang, C.-J.; Shieh, C.-L.; Yin, H.-Y. Laboratory Study of the Underground Sound Generated by Debris Flows. *J. Geophys. Res. Earth Surf.* **2004**, *109*, doi:10.1029/2003jf000048.
79. Kean, J.W.; Coe, J.A.; Coviello, V.; Smith, J.B.; McCoy, S.W.; Arattano, M. Estimating Rates of Debris Flow Entrainment from Ground Vibrations. *Geophys. Res. Lett.* **2015**, *42*, 6365–6372, doi:10.1002/2015GL064811.
80. Huang, C.-J.; Yin, H.-Y.; Chen, C.-Y.; Yeh, C.-H.; Wang, C.-L. Ground Vibrations Produced by Rock Motions and Debris Flows. *J. Geophys. Res.* **2007**, *112*, F02014, doi:10.1029/2005JF000437.
81. Al-fares, W.; Bakalowicz, M.; Guérin, R.; Dukhan, M. Analysis of the Karst Aquifer Structure of the Lamalou Area (Hérault, France) with Ground Penetrating Radar. *J. Appl. Geophys.* **2002**, *51*, 97–106, doi:10.1016/S0926-9851(02)00215-X.
82. Hussain, Y.; Hamza, O.; Cárdenas-Soto, M.; Borges, W.R.; Dou, J.; Rebolledo, J.F.R.; Prado, R.L. Characterization of Sobradinho Landslide in Fluvial Valley Using Masw and Ert Methods. *REM - Int. Eng. Journal.* **2020**, *73*, doi:10.1590/0370-44672019730109.